Combined anterior segment OCT and wavefront-based autorefractor using a shared beam

MARCO RUGGERI,[1,2,*] GIULIA BELLONI,[1,3] YU-CHERNG CHANG,[1,2] HEATHER DURKEE,[1,2] ETTORE MASETTI,[1,3] FLORENCE CABOT,[1,4] SONIA H. YOO,[1,4] ARTHUR HO,[1,5,6] JEAN-MARIE PAREL,[1,2,4,5] AND FABRICE MANNS[1,2]

[1]*Ophthalmic Biophysics Center, Bascom Palmer Eye Institute, University of Miami Miller School of Medicine, Miami, FL 33136, USA*
[2]*Department of Biomedical Engineering, University of Miami College of Engineering, Coral Gables, FL 33146, USA*
[3]*Department of Engineering "Enzo Ferrari", University of Modena and Reggio Emilia, Modena, MO 41125, Italy*
[4]*Anne Bates Leach Eye Center, Bascom Palmer Eye Institute, University of Miami Miller School of Medicine, Miami, FL 33136, USA*
[5]*Brien Holden Vision Institute, Sydney, NSW 2052, Australia*
[6]*School of Optometry and Vision Science, University of New South Wales, Sydney, NSW 2033, Australia*
*mruggeri@med.miami.edu

Abstract: We have combined an anterior segment (AS) optical coherence tomography (OCT) system and a wavefront-based aberrometer with an approach that senses ocular wavefront aberrations using the OCT beam. Temporal interlacing of the OCT and aberrometer channels allows for OCT images and refractive error measurements to be acquired continuously and in real-time. The system measures refractive error with accuracy and precision comparable to that of clinical autorefractors. The proposed approach provides a compact modular design that is suitable for integrating OCT and wavefront-based autorefraction within the optical head of the ophthalmic surgical microscope for guiding cataract surgery or table-top devices for simultaneous autorefraction and ocular biometry.

1. Introduction

Intraoperative wavefront aberrometry and intraoperative OCT are emerging as guidance tools for ocular surgeries. Intraoperative aberrometry provides refractive error measurements in real-time during cataract surgery [1–4]. This technology allows cataract surgeons to confirm intraocular lens (IOL) power choice while the patient remains on the operating table, and to ensure proper alignment of toric IOLs. On the other hand, intraoperative OCT (iOCT) [5–16] enables cross-sectional and volumetric visualization of surgical manipulations in real time with high resolution. In cataract surgery, anterior segment (AS) iOCT [17–19] provides real-time feedback on IOL placement. iOCT and intraoperative aberrometry provide aphakic refraction and biometry, respectively, which could potentially improve IOL power prediction compared to standard calculations based on pre-operative biometry [3,17,18,20,21]. Ideally, cataract surgeons could use AS-iOCT to guide IOL selection and placement and on the same patient fine-tuning refraction with aberrometry. Moreover, iOCT enables verification of the integrity of the anterior segment prior to performing autorefraction to assure reliability of refractive measurements during surgery [22].

Commercial intraoperative OCT devices are integrated within the ophthalmic surgical microscope while intraoperative aberrometers are external modules that are attached under the surgical microscope, interfering with the surgical space [23]. The need to mount and unmount the aberrometer in shared operating rooms affects the surgical workflow. Integrating both technologies within the microscope optical head potentially preserves surgical space and makes the process of intraoperative imaging and aberrometry seamless to the surgeon. A logical solution to the problem of integrating these modalities into the surgical microscope head is combining two separate systems with probing beams operating at different wavelengths, with the OCT beam focused on the anterior segment to optimize image contrast and the aberrometer beam focused on the retina to optimize wavefront sensing. We and other have demonstrated combined AS-OCT and aberrometry [24–26] using a dual-beam approach to study accommodation. However, implementing this approach within the optical head of the surgical microscope is challenging. It requires two separate light sources and the insertion of beam combining optics within the constrained environment of the microscope optical head.

Performing OCT imaging and aberrometry with the same probing beam would significantly simplify optical design and integration of these technologies within the surgical microscope and reduce cost. OCT imaging and aberrometry using a shared beam is commonly performed in adaptive optics (AO) retinal OCT systems [27–29]. In AO-OCT, a narrow parallel beam is focused on the retina to optimize both wavefront sensing and retinal imaging. Nevertheless, AS-OCT requires the beam to be focused on the crystalline lens to obtain images of the anterior segment with high contrast [30,31]. A design with adjustable focus [15,32] could be used to switch beam geometry between modalities. Dynamic focus adjustment can be implemented using electromechanical systems [32] and/or electrically tunable lenses [15]. However, these designs further complicate the integration of the OCT and aberrometer within a surgical microscope.

We have recently developed a combined OCT imaging system and ray tracing aberrometer using an approach that senses wavefront aberration using the OCT beam [33]. The system is designed for studying human and primate crystalline lenses *in vitro*. The probing beam is focused on the crystalline lens to obtain OCT images with high contrast and defocused at the camera sensor of the ray tracing aberrometer. Although we have shown that aberration of the crystalline lens can be accurately measured with a defocused beam at the sensor, the system is designed for *in vitro* applications and cannot be directly translated for *in vivo* use.

In this paper, we explore a new design to perform AS-OCT and wavefront-based autorefraction *in vivo* using a single beam with fixed geometry. Instead of combining two separate devices, we merge the two modalities within one system that uses a single light source and beam delivery system with two separate detection channels to generate both AS-OCT images and wavefront-based refraction. The probing beam is focused within the anterior segment to optimize image quality and defocused at the retina. To demonstrate the feasibility of the approach, we have developed a table-top system that combines a custom-made extended depth AS-OCT system and a custom-made Shack-Hartmann (S-H) based autorefractor with large dynamic range. Refraction obtained with the wavefront-based autorefractor was compared to that obtained with a clinical autorefractor. Temporally interlaced OCT images and refractive error measurements were acquired dynamically on human subjects during accommodation to show that the system can measure changes in refraction and display OCT images continuously and in real time.

2.　System for combined OCT imaging and wavefront-based autorefraction

Figure 1-(A) shows a schematic of the system. The combined OCT-aberrometer uses a custom-made SD-OCT system. The light source is a superluminescent diode (SLD) with a center wavelength of 840 nm and a FWHM (full width at half maximum) bandwidth of 50 nm (cBLMD-S-371-HP3-SM-840-I, Superlum diodes Ltd, Moscow, Russia). The axial resolution of the system is 8 μm in air. The configuration of the spectrometer and interferometer has been described in

our previous work [30,31]. The spectrometer enables imaging at a speed of 20,000 A-lines/s over an axial range of 10.4 mm in air. In this work, a 1×2 MEMS-based fiber-optics switch (OSW12-830E, Thorlabs) was built in the reference arm of the OCT system to extend the axial range to the full anterior segment. The two outputs of the optical switch are interfaced to two optical delay lines consisting of a collimator (A375TM-C f = 7.5 mm, Thorlabs) and mirror (05D20ER.2, Newport) each. The optical path mismatch between the two delay lines was set to achieve a total imaging depth of 13.5 mm in air, which is sufficient to image the full depth of the anterior segment. The OCT beam delivery system consists of a transverse galvanometric scanning device with two axes and optics (L1, AC254-100-B, Thorlabs) that focus the collimated OCT beam (A375TM-C f = 7.5 mm, Thorlabs) near the anterior crystalline lens surface to generate high-contrast OCT images. The focused beam has a diameter of 67 μm at the waist and a depth of focus (two times the Rayleigh range) of 8.4 mm in air. The average power delivered to the eye is 1.6 mW, which is within the maximum permissible exposure according to the ANSI Z80.36-2016 safety standard.

A pellicle beam splitter (BP108, Thorlabs) positioned in front of the beam delivery system (BS1) collects 92% of the light returning from the anterior segment into the OCT system and 8% of the light returning from the retina into the aberrometer. In the aberrometer channel, a 4f relay telescope (L4, L5; AC254-100-B, Thorlabs) images the pupil of the subject onto the lenslet array of a commercial Shack-Hartmann (S-H) wavefront sensor (WFS150-5C, Thorlabs, Newark, NJ). An aperture conjugated with the retina is placed in the aberrometer channel to reduce the effect of corneal reflections. The key difference with conventional S-H aberrometer designs is that the beam reaching the retina is defocused (Fig. 2(A)), with an approximate beam diameter estimated using a OpticStudio (Zemax, Kirkland WA) simulation that varies between 372 and 279 μm for refraction errors ranging in sphere between −10 D and +5 D (phakic eye), and between 375 and 282 μm for refractive errors ranging in sphere between +5 D to +17D (aphakic eye) (Fig. 2(B)). The defocused spot on the retina also causes larger conjugated spots in the Shack-Hartmann sensor, with a diameter that varies between approximately 86 and 111 μm for both the phakic and aphakic eye (Fig. 2(B)).

An accommodation target [30,31] is combined to the OCT channel with a dichroic mirror to relax patient's accommodation during imaging and refractive measurements. A pupil camera consisting of a CCD monochromatic sensor (CMLN-13S2M-CS, Point Grey, Richmond, Canada) and an objective lens (L6; C2514-M, f = 25 mm, Pentax) is combined to the aberrometer channel using a pellicle beam splitter (BS2; CM1-BP108, Thorlabs) to facilitate pupil centration during measurements. A ring of infrared LEDs is used to provide relatively uniform illumination of the anterior segment during alignment with the pupil camera.

Software was developed (LabView) to process and display the OCT images and refraction measurements, and to synchronize the operations of all sub-systems, including the OCT spectrometer, the optical switch, the S-H sensor, the pupil camera and the LED illuminator (Fig. 1(B)). To optimize the contrast of the S-H spot array images, a closed-loop control system dynamically adjusts the exposure time of the wavefront sensor from 1 to 65 ms during wavefront data acquisition (Fig. 1(B)). The wavefront was reconstructed in real time from spot array images using the algorithm provided by the manufacturer of the wavefront sensor (Thorlabs, Inc.). Once the wavefront was reconstructed, sphero-cylindrical refraction (sphere, cylinder and axis) was calculated from the second order Zernike coefficients and displayed in real time.

The combined system is synchronized such that refraction measurements are acquired interlaced with OCT frames at a rate of 4.7 Hz and with a 50% duty cycle. During OCT imaging the beam scans the anterior segment and during wavefront sensing the beam is steady within the pupil (Figs. 1(B), 1(C)). During wavefront sensing, the beam is positioned in the right upper quadrant of the pupil with an offset of 0.5 mm along the horizontal and vertical directions with respect to the pupil center to reduce the intensity of corneal reflections within the aberrometer channel. The
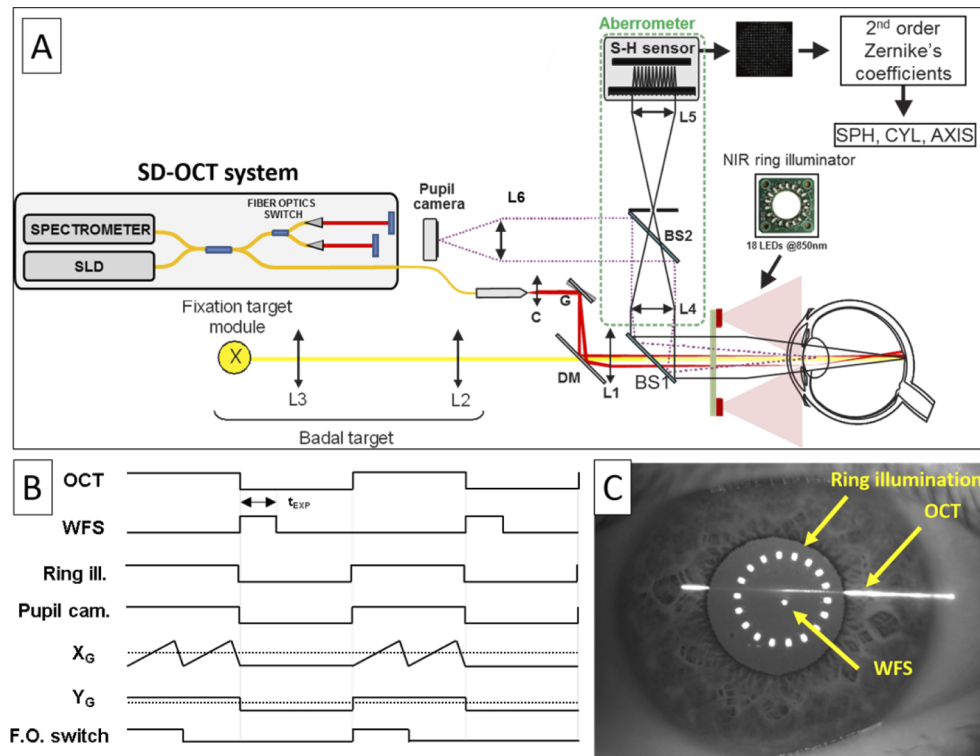
Fig. 1. (A) Schematic of the system for combined OCT imaging and Shack-Hartmann aberrometry using a single beam. The OCT system with interferometer, light source (SLD), spectrometer, reference arm with fiber optics switch is shown. The optical components of the beam delivery unit are labelled: G, dual axis scanning mirrors; C, collimator, L1, objective lens; L2, L3 Badal target lenses; L4, L5 4f relay system, L6, camera objective lens, DM, dichroic mirror; BS1, BS2 pellicle beam splitters. OCT probing beam is shown in red, optical path of the S-H aberrometer is shown in black, optical path of the alignment camera is shown in magenta and optical path of the fixation target is shown in yellow. (B) Timing diagram of the system operation. The system is synchronized such that wavefront measurements are acquired interlaced with the OCT frames and pupil images. The ring illuminator is inactive during wavefront sensing to avoid light back-reflected from the anterior segment to affect wavefront measurements. Exposure time of the wavefront sensor (t_{exp}) is controlled in a closed-loop fashion between 1 and 65 ms. Typical shape of the driving signals of the horizontal and vertical scanners (X_G and Y_G) are reported for an horizontal OCT scan. The horizontal scanner (X_G) is synchronized with the fiber optics switch so that two OCT images at different depth are consecutively acquired and combined to extend the imaging range. In the example, the signal driving the vertical scanner (Y_G) is set at two different constant offsets for the OCT and wavefront sensing modes, corresponding to two different vertical positions in the eye. (C) Image captured with the pupil camera showing the corneal reflections generated by the scanning beam during OCT and wavefront sensing and by the ring illuminator. In this example, an offset (0.8×0.3 mm, horizontal $\times$ vertical) between the locations of OCT imaging and wavefront sensing (WFS) was introduced to separately display the scanning beam during the two sensing modes.
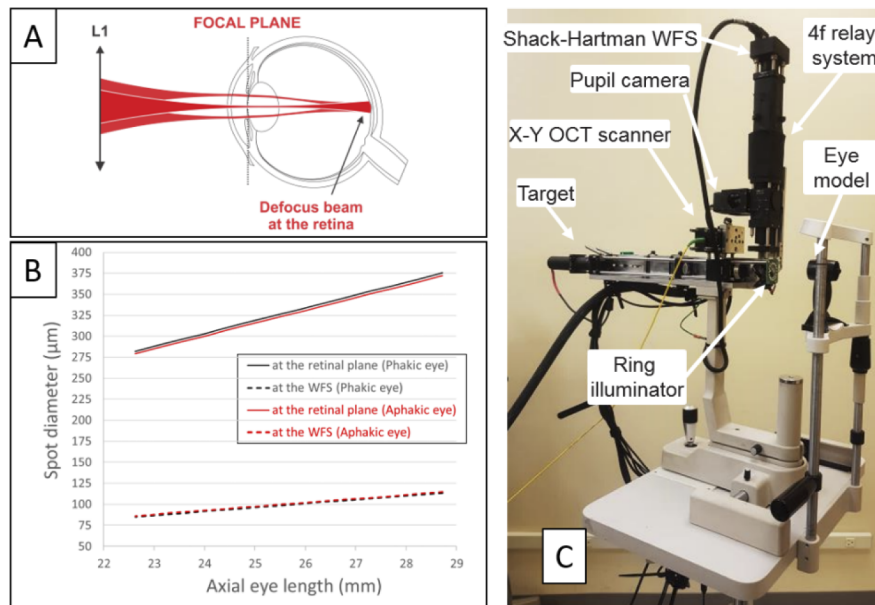
Fig. 2. (A) Representation of the system illumination with the probing beam scanning transversally across the emmetropic eye. For the emmetropic eye, the scanning beam converges to the same location on the retina. The beam is focused by the objective lens (L1) near the iris plane to optimize OCT imaging and is defocused at the retina. (B) Diameter of the extended spot at the retina in the phakic and aphakic eye (solid lines) and at the wavefront sensor (dashed lines) as a function of axial eye length. The extended spot diameter was calculated by varying the axial eye length of a common computational model eye [34] between 22.6 and 28.7 mm to control the amount of defocus between −10 D and +5 D for the phakic eye (black lines) and between +5 and +17 D for the aphakic eye (red lines). (C) Photograph of the integrated system mounted on a table-top with headrest. An eye model is positioned on the head rest at a working distance of approximately 60 mm from the system.

integrated OCT-aberrometer delivery system and fixation target are mounted on an ophthalmic table equipped with joystick and headrest to perform experiments on human subjects (Fig. 2(C)).

3. Experiments

A series of experiments were performed to: 1) test the ability of the wavefront-based autorefractor to produce accurate and repeatable refraction measurements using a defocused beam on an physical eye model, 2) evaluate the accuracy and intra- and inter-session repeatability of refractive measurements on 14 human subjects and 3) test the basic proof of concept of the wavefront-based aberrometer using a defocused beam to measure refraction and display OCT images continuously and in real time in two human subjects.

3.1. Testing and validation of the wavefront-based autorefractor on a model eye

The accuracy and dynamic range of the S-H based autorefractor was evaluated using a model eye that consists of an achromatic doublet lens with a focal length of 30 mm positioned in front of the diffuse reflector of an integrating sphere port plug (Labsphere). The reflector is mounted to a translation stage to allow for axial displacement, mimicking the spherical error of the eye. The model eye has a 4 mm diameter iris placed behind the achromatic doublet. To determine the

dynamic range, the translation stage was adjusted in 1 mm steps to mimic myopic and hyperopic defocus shifts corresponding to a total of 52 refractive error steps ranging in sphere between −17 D and +25 D. Wavefront data was recorded for each position. To confirm the ability of the system to measure astigmatism over a large defocus range, additional experiments were performed with 9 cylindrical trial lenses from a standard optometrist's kit (CYL: −5, −4, −3, −2, −1, +1, +2, +3, +4 and +5D) placed at 7 mm in front of the anterior surface of the achromat. For each trial lens, measurements were repeated at four different axes (0, 45, 90 and 135°) and in combination with five values of sphere (−16, −8, 0, +8 and +16D) obtained by displacing the diffusive surface, for a total of 180 sphero-cylinder combinations. Wavefront data was recorded for each combination of induced sphere, cylinder and axis.

To assess repeatability, all measurements were repeated three times, for a total of 540 measurements. Accuracy of the measurements was verified by comparing the refraction measured with the wavefront-based autorefractor with refraction predicted using an optical simulation of the eye model based on thin lenses and paraxial optics. The optical simulation takes into account the distance between the cylindrical trial lens and the achromat.

3.2. Accuracy and repeatability of refraction measurements on human eyes

Following an Institutional Review Board approved protocol, experiments were performed on 28 eyes of 14 subjects ranging in age from 20 to 70 years (32.9 ± 14.3 years) with mean spherical equivalent (M) between −9.4 to +1.6 D. All subjects provided written informed consent. Refractive error was measured on both eyes of every subject without the use of cycloplegia. Subjects were first measured with a clinical autorefractor (KR-800, Topcon). Five consecutive measurements were taken for each eye without repositioning the system between measurements. The five measurements took less than 10 seconds. Wavefront data was acquired with the custom-made autorefractor after adjustment of the fixation target to the subject's far point to relax accommodation [30]. The sampling pupil was fixed to 2 mm diameter and centered to the area of the wavefront sensor. The custom-made autorefractor was programmed to acquire ten consecutive measurements for each eye in less than 1 second. The average refractive error measured by each instrument was then calculated in power vector notation including mean spherical equivalent (M) and vertical and oblique Jackson cross-cylinders (J0 and J45) [35,36]. Vertex distance correction (16.5 mm) was applied to the wavefront-based measurements to calculate refraction in the same spectacle plane used by the clinical autorefractor. Agreement between the wavefront-based and commercial autorefractor was evaluated for the mean values of M, J0 and J45 using a Bland-Altman analysis [37].

Power vector measurements with the custom-made autorefractor using the same protocol described above were repeated five times on both eyes of three subjects of age 25, 28 and 43 years to assess intra-session variability. The subject head was repositioned between measurements. To assess inter-session repeatability, five measurements using the same protocol as described above were repeated at 30 minutes intervals on the same three subjects.

### 3.3. Real-time autorefraction and anterior segment OCT imaging

Interlaced OCT images and refractive error measurements were acquired dynamically at 4.7 Hz in the right eye of two subjects (23 and 43 years) responding to a variable stimulus in accommodation. The accommodation target was manually adjusted to provide a stimulus amplitude of 4 D in the direction of accommodation while OCT images and wavefront measurements were acquired. Before acquisition, the accommodation target was adjusted to the subject's far-point to relax accommodation and the manual stimulus was presented after approximately 1 s from the beginning of an acquisition for a total duration of approximately 4 s. Each OCT image consisted of 720 × 2667 pixels (horizontal × vertical) over a lateral width of 14 mm and a depth of 13.45 mm (in

air). Wavefront data was acquired with the S-H autorefractor over a sampling pupil of 2 mm in diameter and centered to the area of the wavefront sensor.

4. Results

4.1. Autorefractor performance on the model eye

Figure 3(A) shows the dynamic range of the wavefront-based autorefractor measured on the model eye. The measured defocus varies linearly with the simulated defocus over the range between −17 and +25D. The optical power at the wavefront sensor was too low to be able to measure sphere values below −17D, while mechanical constrains in the eye model limited the positive sphere range to +25D. The difference between measured spherical power and the power induced by the eye model was less than 0.35 D across the full range (Fig. 3(B)). The absolute error between repeated sphere power measurements was less than 0.01 D in all cases. A distinct convex profile in the residual sphere power error can be observed in Fig. 3(B). This convex profile might arise from a shift in the relative position of the S-H sensor with respect to the exit pupil of the eye model which could be corrected. For example, the standard error of the 2nd-order polynomial fit in Fig. 3(B) suggests the mean difference between measured and simulated sphere power may be reduced to below 0.09 D.
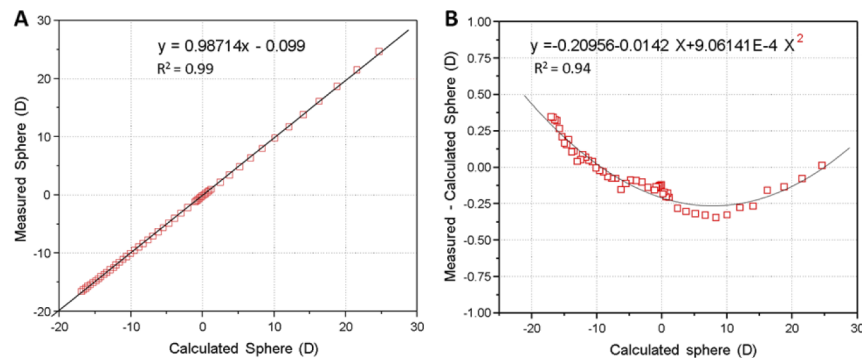

Fig. 3. (A) Comparison between wavefront-based sphere measurements and calculated values of sphere induced by the eye model. Each symbol (red) represents the mean of 3 measurements. Linear fit of the data samples and R^2 coefficient are displayed (black). (B) Difference between wavefront-based sphere measurements and calculated sphere. Second order polynomial fit of the data samples and R^2 coefficient is displayed (black).

Figure 4 shows the comparison between measured and predicted sphere and cylinder in all runs. For 0 D spherical error, the error in cylinder prediction is less than 0.25 D for the 5 D range cylinder. For sphere powers within ±16 D, the maximum absolute difference in average sphere and cylinder across three runs and four axes (Table 1) is 0.51 D. These errors are within the expected limits of accuracy of the paraxial thin lens model used to predict refraction at the ends of the range (±16 D). Repeated measurements (three repeated measurements for nine cylinder powers and four cylinder axes) were all within 0.31 D and 0.21 D for sphere and cylinder, respectively, with average standard deviations of 0.05 D and 0.09 D (Table 1), respectively, suggesting that the measurements on the eye model are highly reproducible.

4.2. Autorefractor performance on the human eye

Table 2 reports the results of repeated power vector measurements for both eyes of the 24, 28 and 43 year-old subjects. Standard deviation of the intra-session repeated measurements is within 0.20, 0.07 and 0.16 D from the mean values of M, J0 and J45, respectively, or, equivalently,
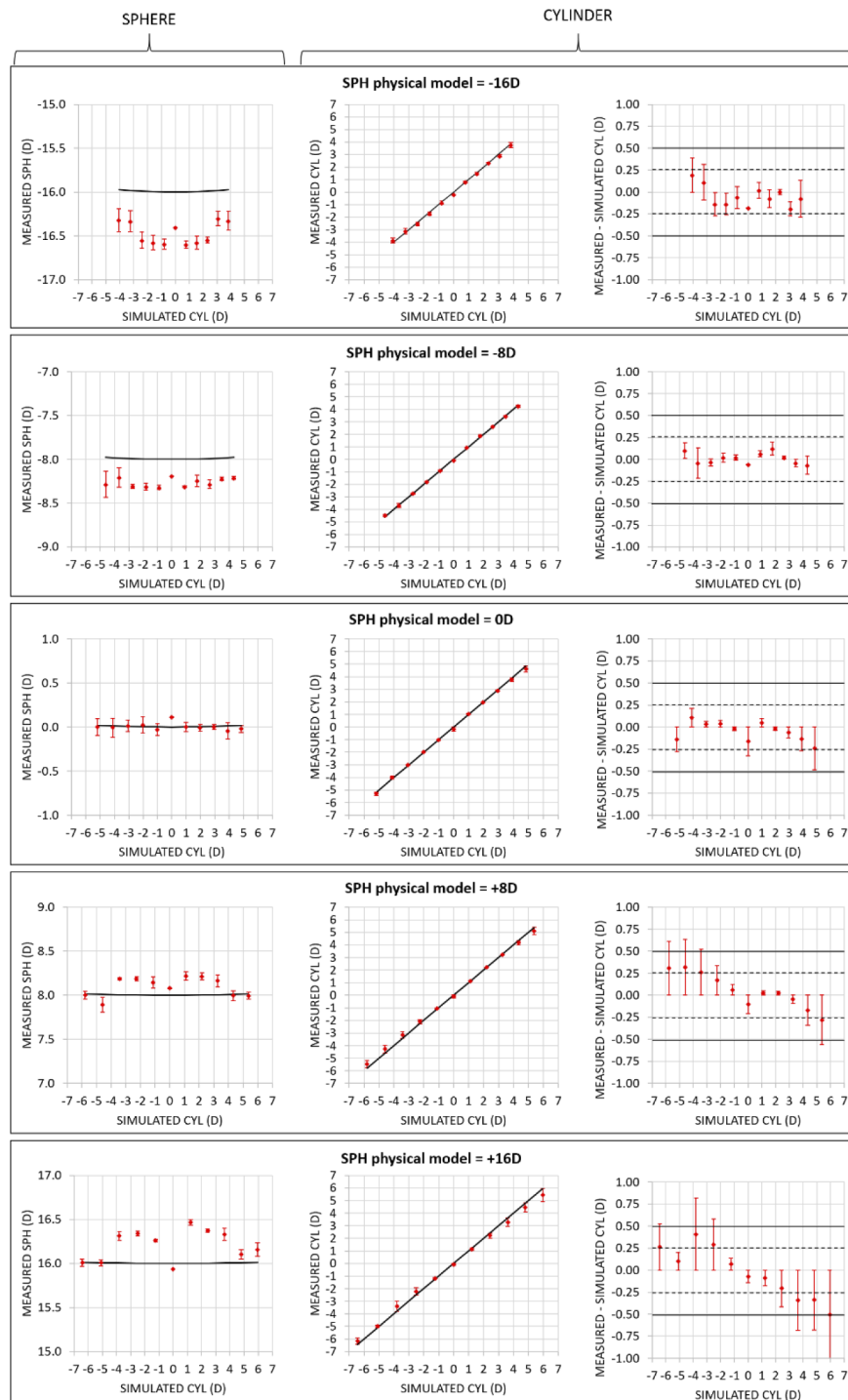
Fig. 4. (Left and central columns) Correlation between measured (red) and simulated (black) sphere and cylinder powers. Each symbol in the graphs show the mean value of 12 measurements (3 repeated measurements for 3 cylindrical axes) versus 9 simulated cylinder powers (horizontal axis) for a total of 5 simulated sphere powers (−16, −8, 0, +8, +16 D). Error bars refer to the standard deviation over the 12 measurements. The lines of perfect correlation are reported (black). (Right column) Difference between measured and simulated cylinder powers. Vertical limits for ±0.25 D (dashed line) and ±0.50 D (solid line) are indicated.

Table 1. Maximum absolute difference between predicted and measured sphere and cylinder and average standard deviations of the measurements[a]

		Simulated sphere (D)				
		−16	−8	0	+8	+16
Maximum absolute error (D)	Sphere	0.60	0.32	0.11	0.22	0.47
	Cylinder	0.19	0.12	0.24	0.32	0.51
Average Standard Deviation (D)	Sphere	0.07	0.05	0.06	0.04	0.04
	Cylinder	0.12	0.06	0.10	0.07	0.09

[a]all values are calculated across 108 measurements (three repeated measurements for nine cylinder powers and four cylinder axes)

within 0.10 and 0.24 D for sphere and cylinder, respectively, and within 14° for the axis. For the inter-session repeatability, standard deviation is within 0.35, 0.15 and 0.12 D from the mean values of M, J0 and J45, respectively, or, equivalently, within 0.28 and 0.20 D for sphere and cylinder, respectively, and within 12° for the axis. In each run of the repeated measurements, the refractive error was calculated as the average of ten consecutive measurements acquired in less than 1 second.

Table 2. Intra-session and inter-session repeatability[a]

Subject	Power Vector	Intra-session Mean ± STD [Range]		Inter-session Mean ± STD [Range]	
		OD	OS	OD	OS
24 y/o	M (D)	−0.96 ± **0.20** [−1.12,−0.63]	−1.10 ± **0.14** [−1.32,−0.96]	−1.00 ± **0.15** [−1.23,−0.84]	−0.87 ± **0.18** [−1.18,−0.73]
	J0 (D)	−0.26 ± **0.07** [−0.35,−0.16]	−0.23 ± **0.02** [−0.27,0.21]	−0.08 ± **0.12** [−0.27,0.06]	−0.21 ± **0.05** [−0.27,−0.13]
	J45 (D)	−0.23 ± **0.16** [−0.37,0.05]	0.05 ± **0.04** [−0.02,0.09]	−0.21 ± **0.09** [−0.35,−0.10]	0.04 ± **0.12** [−0.16,0.12]
28 y/o	M (D)	−0.72 ± **0.10** [−0.86,−0.63]	−0.90 ± **0.07** [−1.00,−0.84]	−0.62 ± **0.10** [−0.72,−0.50]	−0.98 ± **0.09** [−1.09,−0.89]
	J0 (D)	0.18 ± **0.03** [0.15,0.22]	−0.05 ± **0.01** [−0.06,−0.04]	0.14 ± **0.05** [0.07, 0.19]	−0.06 ± **0.04** [−0.12,0.00]
	J45 (D)	−0.37 ± **0.06** [−0.45,−0.27]	0.07 ± **0.04** [0.02,0.10]	−0.30 ± **0.07** [−0.40,−0.23]	0.11 ± **0.05** [0.04,0.18]
43 y/o	M (D)	−2.10 ± **0.02** [−2.12,−2.08]	−2.45 ± **0.19** [−2.69,−2.16]	−2.03 ± **0.23** [−2.38,−1.76]	−2.37 ± **0.35** [−2.95,−2.07]
	J0 (D)	−0.22 ± **0.03** [−0.28,−0.20]	0.07 ± **0.05** [0.00,0.11]	−0.12 ± **0.08** [−0.22,−0.00]	0.21 ± **0.15** [0.00,0.36]
	J45 (D)	−0.26 ± **0.02** [−0.27,−0.22]	−0.24 ± **0.06** [−0.31,−0.15]	−0.29 ± **0.07** [−0.40,−0.21]	−0.29 ± **0.12** [−0.43,−0.15]

[a]all values were calculated over 5 repeated measurement runs. In each run, refraction was calculated as the average of 10 consecutive measurements acquired with the wavefront-based autorefractor in less than 1 second.

To evaluate the effect of data averaging on intra- and inter-session repeatability we repeated the calculations by only including the first of the 10 consecutive refractive measurements. We found

similar repeatability with standard deviation within 0.20, 0.08 and 0.16 D from the mean values of M, J0 and J45 for intrasession tests, and within 0.37, 0.18 and 0.15 from the mean values of M, J0 and J45 for intersession tests. Overall, the measurement variability is comparable to that of clinical autorefractors and subjective refraction [38–42]. The results confirm that the system provides sufficient precision to reliably measure refractive error.

Figures 5(A), 5(C) and 5(E) shows the correlation plots between the power vectors (M, J0, and J45) measured with the wavefront-based autorefractor and the clinical autorefractor. Power vectors M and J0 are strongly correlated between the two instruments with Pearson's linear correlation coefficients $r = 0.968$ ($p < 0.001$) and $r = 0.942$ ($p < 0.001$), respectively. Power vectors J45 show a significant but more moderate correlation ($r = 0.42$, $p = 0.025$) than M and J0, which is probably caused by the limited range of J45 values contributing to the linear fit (−0.28 to +0.20 D) for the participating subjects (Fig. 5). Bland-Altman analysis (Figs. 5(B), 5(D) and 5(F)) shows a mean difference (± 95% C.I.) between the power vectors acquired by the two systems of 0.64 (± 2.71), −0.01 (± 0.68) and 0.20 (± 0.83) D for M, J0 and J45, respectively. Compared to the measurement acquired with the clinical autorefractor, the wavefront based system systematically underestimates the magnitude of M in the myopic range (Fig. 5(A)). In the hyperopic range, the number of data points ($n = 3$) collected are insufficient to determine with certainty the systematic behavior of the wavefront-based system with the respect to the clinical autorefractor. Systematic errors are negligible for J0. For J45, measurements with the wavefront autorefractor are on average 0.20 D lower than the measurements acquired with the clinical system. These performances are comparable to those of experimental wavefront based autorefractors using a beam focused at the retina [43,44].

A predictable relation is found between the wavefront-based and commercial autorefractors, suggesting that the measurement accuracy can be improved by using the regression equation or a curve fit as a correction factor for calibration. A further study on a separate study group will be required to validate the calibration.

4.3. Real-time refraction and OCT imaging of the anterior segment

Figure 6 shows the real-time anatomical and optical response produced by the system to a 4D accommodation stimulus in the 23 (Fig. (6), see Visualization 1) and the 43 year-old subject (Fig. (6), see Visualization 2). The movies display OCT images of the anterior segment and refractive error measurements. As the eye accommodates, the OCT images show an increase in thickness and surface curvature of the crystalline lens while the spherical component of refraction becomes more negative, as expected. The experiment demonstrates the ability of the system to continuously display in real time anatomical changes in the anterior segment with OCT and refraction using a single beam.

Two relatively large jumps in refraction (> 1 D in amplitude) were recorded prior to the application of the accommodation stimulus in the 43 year-old subject (Fig. (6)). These variations are isolated and not attributable to accommodation, as also confirmed by the OCT sequence. Based on our experience with S-H aberrometers, we believe these errors were introduced by corneal reflections that interfere with the wavefront measurements. Although the aberrometer was programmed to deliver the probing beam slightly decentered with respect to the corneal apex to avoid reflections, small and rapid eye movements might occur during the wavefront sensing phase of the interlaced mode that could introduce reflections in the aberrometer channel. These subtle eye movements are not necessarily detected in the dynamic 2D OCT sequence since wavefront sensing occurs when OCT imaging is inactive. As further discussed in the next section, the effect of outliers generated by corneal reflections may be mitigated by increasing the acquisition speed of the wavefront sensor so that multiple measurements can be acquired and averaged within a single period of the interlaced acquisition.
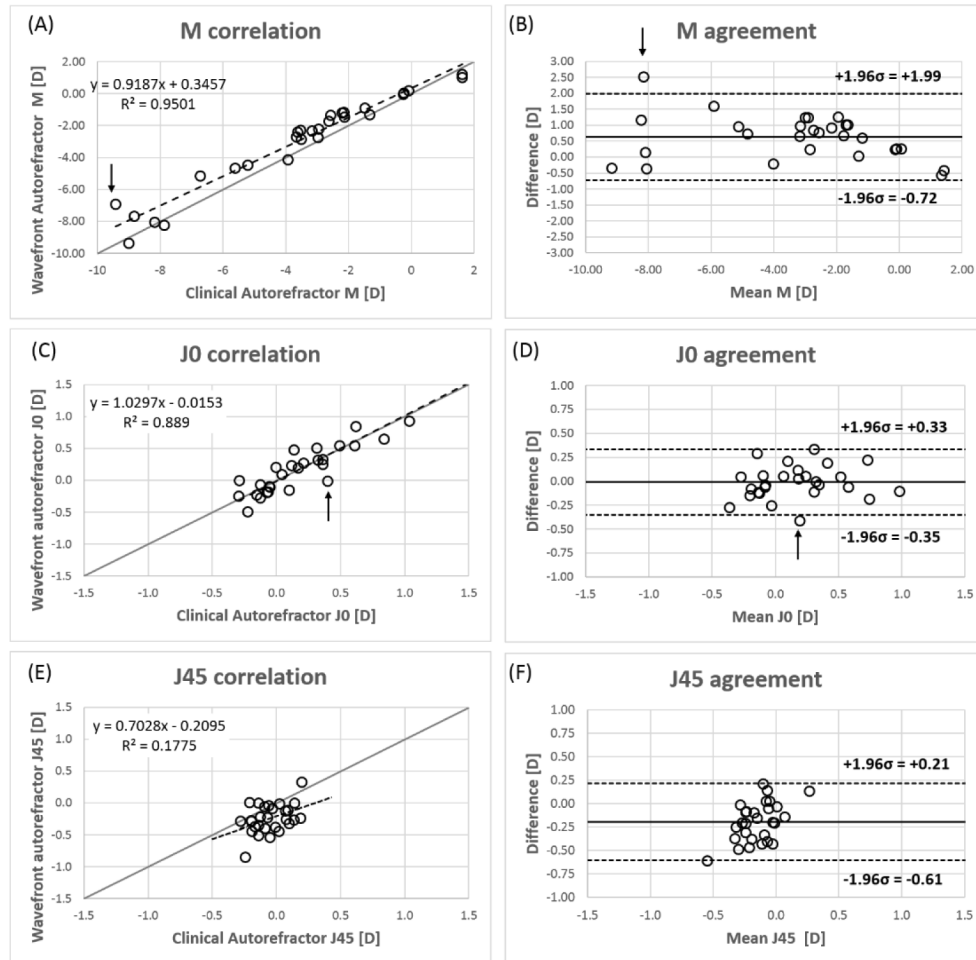
Fig. 5. Correlation plots for M (A), J0 (C) and J45 (E) measured with the wavefront-based autorefractor and the clinical autorefractor. The plots show the mean value of 10 consecutive measurements performed with the wavefront-based autorefractor (vertical axis) versus the mean value of 5 consecutive measurements performed with the clinical autorefractor (horizontal axis). The diagonal (grey line) is the 1:1 line (perfect correlation). Linear fit equation and R^2 coefficient for J0 are displayed. J45 datapoints were not fit as the subjects only span a limited range of values (−0.28 to +0.20 D). Bland-Altman analysis of the agreement between M (B), J0 (D) and J45 (F) measured with the two autorefractors. Two datapoints at the extremity of the myopic range exceeded the limits of agreement for M (OD, age = 52 years, M = −9.4 D) and J0 (OD, age = 20, M = −6.7 D), respectively, and they are likely to be outliers (arrows).
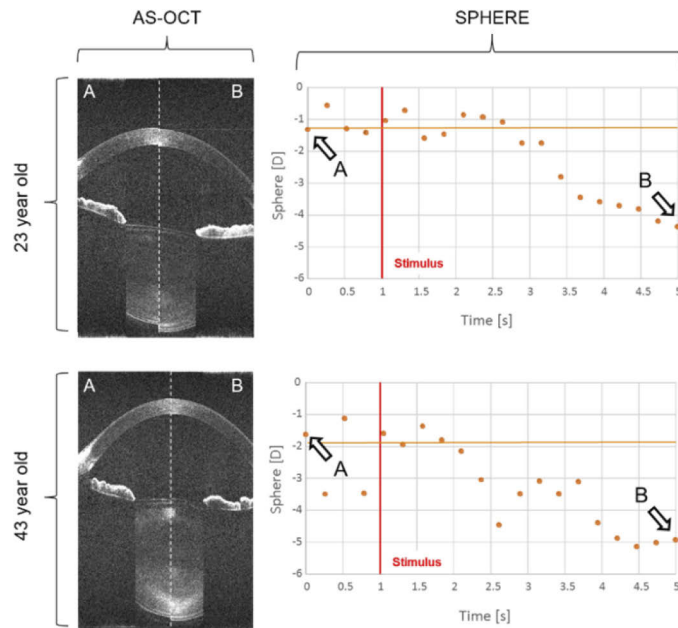
Fig. 6. Real-time display of anterior segment and sphere measurements during accommodation (4 D) in a 23 (see Visualization 1) and a 43 (see Visualization 2) year-old subject with refraction (sphere) of −1.40 and −1.96 D, respectively (orange lines). The OCT images and sphere measurements were acquired at frequency of 4.7 Hz during the accommodative response from the relaxed state (A) to the accommodated (B) state. The measurement variability in the relaxed state of the 43 year-old subject may be due to measurement errors generated by corneal reflections coupling in the aberrometer channel.

5. Discussion

Combining AS-OCT and wavefront-based autorefraction intraoperatively could significantly enhance surgical guidance in cataract surgery. As a preliminary step toward the development of an intraoperative system combining these modalities, we demonstrated the proof of principle of combined AS-OCT imaging and Shack-Hartmann wavefront sensing using a single shared beam. Systems for simultaneous AS-OCT imaging and wavefront sensing have been developed by combining two separate devices with probing beams operating at different wavelengths and with different beam geometries [24–26]. We propose a new approach that uses a single beam with fixed geometry to perform both AS-OCT imaging and wavefront sensing. A key advantage of this approach is that a shared light source and beam delivery optics can be used, simplifying alignment and allowing for a simpler and more compact layout suitable for integrating the two modalities within the optical head of the surgical microscope while reducing cost.

There are two main technical challenges with the proposed shared beam design. Wavefront sensing is generally performed by formation of a focused spot in the retina using a parallel beam entering the eye and sensing of the wavefront distortions produced during the beam's return passage. We proposed an alternative beam geometry to detect wavefront distortion using a beacon beam focused at the anterior segment and defocused at the retina, which is optimized for AS-OCT imaging but not for wavefront sensing. The first challenge of this design was to determine a beam geometry that produces an acceptable trade-off between OCT image quality and reliable wavefront-based refraction measurements. The spot size in the anterior segment must be small to produce OCT images with acceptable lateral resolution. At the same time, the

retinal spot size should be less than the size of the isoplanatic patch [45–49] to avoid wavefront measurement errors. The defocused spot on the retina also causes larger conjugated spots in the Shack-Hartmann sensor, which must be sufficiently displaced to avoid the enlarged spots in the Shack-Hartmann image to merge, causing difficulties in detecting their centroids when reconstructing the wavefront. We identified a beam geometry (NA = 0.008) that together with the optical design of the aberrometer channel satisfies all these conditions. With a spot size at the beam waist of 67 μm and a depth of focus of 8.4 mm the system generates OCT images with high contrast along the entire length of the anterior segment. With this beam geometry, optical simulations (OpticStudio, Zemax) show that the retinal spot size is comparable for the phakic (M ranging from −10 to +5 D) and aphakic (M ranging from +5 to +17 D) eye and ranges approximately between 280 and 375 μm, which is within or comparable to the isoplanatic patch depending on the reference value used for the size of the patch [45–49]. We verified experimentally on a physical eye model that the extended retinal spots generate conjugated spots in the Shack-Hartmann image that are sufficiently displaced to avoid merging over a large range of refractive errors (M between −17 D and +25 D). We therefore expect no refraction errors due to the isoplanatic patch limitation and to the extended spot size at the S-H sensor within the range of ±17 D (M), as also confirmed by the high accuracy obtained when measuring the refractive error induced by the physical eye model.

Another challenge of the shared beam design was the integration of the aberrometer within the optical path of the OCT delivery system, which produces a loss of power in the OCT channel reducing the signal-to-noise ratio of the OCT images. A trade-off between the minimum power required for reliable wavefront reconstruction, minimum power required for OCT imaging, and maximal power allowable to remain within safe exposure limits was found by delivering an optical power of 1.6 mW to the eye while splitting 92% of the returning light in the OCT channel and 8% percent in the aberrometer channel. Although the optical power of the beam is relatively high compared to conventional OCT systems operating at 840 nm (1.6 mW vs. 0.75 mW) [50], the irradiance produced at the anterior segment and retina with the selected optical power and beam geometry falls within the maximum permissible exposure calculated according to the ANSI Z80.36-2016 safety standard (i.e. 2.4 mW).

Unlike with dual-beam systems, the proposed approach facilitates compliance with safety standards as only one beam is used to illuminate the eye. Nevertheless, wavefront measurements and OCT images cannot be acquired simultaneously with the proposed single-beam design since the beam must be scanned across the pupil for OCT imaging while it must be stationary during wavefront sensing. We have shown that interlaced acquisition enables displaying both OCT images and refractive measurements continuously at a speed of 4.7 Hz, which is sufficiently fast for real-time applications in the operating room. Alternatively, the system could be reprogrammed so that the user can select to operate one modality at the time at full acquisition rate (9.4 Hz). The choice of a higher optical power within the safety standard limits could increase the signal-to-noise ratio (SNR) of the Shack-Hartmann and OCT images, possibly allowing a proportionate increase in speed during interlaced synchronization. Higher SNR of the Shack-Hartmann images could be also achieved using a wavefront sensor with higher spectral sensitivity in the NIR region around 840 nm and/or a lenslet array with a larger pitch and smaller number of lenslets, if only sphere and defocus are desired. Whether individually or combined, these strategies to increase SNR and speed will enable averaging multiple refraction measurements per period during interlaced operation, potentially making refraction less vulnerable to isolated measurement errors such as those generated by corneal reflections (Fig. (6)). The effect of corneal reflections is generally mitigated using combinations of polarizers in the illumination and detection paths of the S-H aberrometer. However, in our setup, the use of polarizers in the OCT path might affect the quality of the OCT images. Another solution to increase speed during interlaced operations is by upgrading the SD-OCT system with faster OCT technology, like swept source (SS) OCT.

SS-OCT allows for more than an order of magnitude improvement in imaging rate over our OCT system. A drawback of swept lasers for anterior segment and retinal OCT imaging is that they generally operate in the spectral region around 1 μm, where the spectral responsivity of the silicon detectors commonly used in wavefront sensors is greatly reduced. As a result, a wavefront sensor with increased sensitivity in the spectral region around 1 μm might be needed to obtain reliable wavefront measurements with the beam of a SS-OCT system.

Autorefraction based on Shack-Hartmann wavefront sensing was chosen as it enables high measurement rates [43,44]. In principle, the proposed shared-beam design can be adapted to other wavefront reconstruction techniques such as laser ray tracing, as suggested by our previous findings on ray tracing aberrometry of the crystalline lens *in vitro* using a defocused beam [33].

Precision and accuracy of the autorefractor was assessed on a model eye that provides controlled amount of defocus between −17 and +25 D and cylinder in the ± 5 D range and in 28 eyes of 14 patients with spherical equivalent ranging between approximately −10 to +2 D. The precision of the autorefractor (standard deviation of the measurements within 0.28 D, 0.20 D and 14°, for sphere, cylinder and axis, respectively) is comparable to those of commercial autorefractors and subjective refraction [38–42].

Comparison against a commercial autorefractor suggests that the measurement accuracy of the wavefront-based autorefractor is comparable to those of experimental wavefront based autorefractors using a beam focused at the retina [43,44]. Ultimately, we expect that the accuracy can be further improved by using a curve fit of the measurement error as a correction factor for calibration. To make further progress, a larger number of eyes should be used to assess accuracy and calibrating the system to account for a wider range of refractive errors and eye conditions. For example, subjects with cataracts, large high-order aberrations (e.g. post-refractive surgery eyes) and pseudophakia should also be studied to assess whether the system can reliably measure refraction in these conditions. Cataracts and ocular aberrations might decrease the power and quality of the illumination beam, which further complicates detection of the spot centroids in the Shack-Hartmann image, affecting wavefront reconstruction and reliability of the measurements. Validation on the pseudophakic eye is also important to establish if the system can confirm refractive outcomes after IOL implantation. Ultimately, integration of the technology in the ophthalmic microscope will enable validation of the approach in the aphakic eye. Although we have demonstrated that refractive error can be measured with a defocused beam, it remains to be established whether this approach provides enough accuracy to reliably measure higher-order aberrations.

Disclosures. The University of Miami and some of the authors (MR, FM, JMP and HD) stand to benefit from intellectual property in the technology used in this study.

Data availability. Data underlying the results presented in this paper are not publicly available at this time but may be obtained from the authors upon reasonable request.

References

1. A. P. Canto, P. Chhadva, F. Cabot, A. Galor, S. H. Yoo, P. K. Vaddavalli, and W. W. Culbertson, "Comparison of IOL power calculation methods and intraoperative wavefront aberrometer in eyes after refractive surgery," J. Refract. Surg. **29**(7), 484–489 (2013).
2. A. T. Epitropoulos, "Visual and refractive outcomes of a toric presbyopia-correcting intraocular lens," J. Ophthalmol. **2016**, 1–6 (2016).
3. T. Ianchulev, J. Salz, K. Hoffer, T. Albini, H. Hsu, and L. Labree, "Intraoperative optical refractive biometry for intraocular lens power estimation without axial length and keratometry measurements," J. Cataract Refractive Surg. **31**(8), 1530–1536 (2005).

4. M. Packer, "Effect of intraoperative aberrometry on the rate of postoperative enhancement: retrospective study," J. Cataract Refractive Surg. **36**(5), 747–755 (2010).
5. J. P. Ehlers, W. J. Dupps, P. K. Kaiser, J. Goshe, R. P. Singh, D. Petkovsek, and S. K. Srivastava, "The prospective intraoperative and perioperative ophthalmic imaging with optical coherence tomography (PIONEER) Study: 2-year results," Am. J. Ophthalmol. **158**(5), 999–1007.e1 (2014).
6. J. P. Ehlers, J. Goshe, W. J. Dupps, P. K. Kaiser, R. P. Singh, R. Gans, J. Eisengart, and S. K. Srivastava, "Determination of feasibility and utility of microscope-integrated optical coherence tomography during ophthalmic surgery: the DISCOVER study RESCAN results," JAMA Ophthalmol. **133**(10), 1124–1132 (2015).
7. G. Geerling, M. Müller, C. Winter, H. Hoerauf, S. Oelckers, H. Laqua, and R. Birngruber, "INtraoperative 2-dimensional optical coherence tomography as a new tool for anterior segment surgery," Arch. Ophthalmol. **123**(2), 253–257 (2005).
8. T. Ide, J. Wang, A. Tao, T. Leng, G. D. Kymionis, T. P. O'Brien, and S. H. Yoo, "Intraoperative use of three-dimensional spectral-domain optical coherence tomography," Ophthalmic Surg. Lasers Imaging Retina **41**(2), 250–254 (2010).
9. P. B. Knecht, C. Kaufmann, M. N. Menke, S. L. Watson, and M. M. Bosch, "Use of intraoperative fourier-domain anterior segment optical coherence tomography during descemet stripping endothelial keratoplasty," Am. J. Ophthalmol. **150**(3), 360–365.e2 (2010).
10. E. M. Lankenau, M. Krug, S. Oelckers, N. Schrage, T. Just, and G. Hüttmann, "iOCT with surgical microscopes: a new imaging during microsurgery," Adv. Opt. Technol. **2**(3), 233–239 (2013).
11. M. Ruggeri, F. Cabot, S. H. Yoo, and J.-M. Parel, "Evaluation of a surgical microscope interfaced SD-OCT system for anterior segment surgery," Invest. Ophthalmol. Vis. Sci. **56**(7), 4088 (2015).
12. V. Scorcia, M. Busin, A. Lucisano, J. Beltz, A. Carta, and G. Scorcia, "Anterior segment optical coherence tomography-guided big-bubble technique," Ophthalmology **120**(3), 471–476 (2013).
13. P. Steven, C. Le Blanc, E. Lankenau, M. Krug, S. Oelckers, L. M. Heindl, U. Gehlsen, G. Huettmann, and C. Cursiefen, "Optimising deep anterior lamellar keratoplasty (DALK) using intraoperative online optical coherence tomography (iOCT)," Br. J. Ophthalmol. **98**(7), 900–904 (2014).
14. Y. Tao, M. LaBarbera, J. P. Ehlers, S. K. Srivastava, and W. J. Dupps, "Image-guided modified deep anterior lamellar keratoplasty (DALK) corneal transplant using intraoperative optical coherence tomography," Invest. Ophthal. Vis. Sci. **56**(7), 1966 (2015).
15. Y. K. Tao, S. K. Srivastava, and J. P. Ehlers, "Microscope-integrated intraoperative OCT with electrically tunable focus and heads-up display for imaging of ophthalmic surgical maneuvers," Biomed. Opt. Express **5**(6), 1877–1885 (2014).
16. O. M. Carrasco-Zevallos, B. Keller, C. Viehland, L. Shen, G. Waterman, B. Todorich, C. Shieh, P. Hahn, S. Farsiu, A. N. Kuo, C. A. Toth, and J. A. Izatt, "Live volumetric (4D) visualization and guidance of in vivo human ophthalmic surgery with intraoperative optical coherence tomography," Sci. Rep. **6**(1), 31689 (2016).
17. N. Hirnschall, S. Amir-Asgari, S. Maedel, and O. Findl, "Predicting the postoperative intraocular lens position using continuous intraoperative optical coherence tomography measurements," Invest. Ophthalmol. Visual Sci. **54**(8), 5196–5203 (2013).
18. N. Hirnschall, S. Norrby, M. Weber, S. Maedel, S. Amir-Asgari, and O. Findl, "Using continuous intraoperative optical coherence tomography measurements of the aphakic eye for intraocular lens power calculation," Br. J. Ophthalmol. **99**(1), 7–10 (2015).
19. L. M. Lytvynchuk, C. G. Glittenberg, C. I. Falkner-Radler, B. Neumaier-Ammerer, E. Smretschnig, S. Hagen, S. Ansari-Shahrezaei, and S. Binder, "Evaluation of intraocular lens position during phacoemulsification using intraoperative spectral-domain optical coherence tomography," J. Cataract Refractive Surg. **42**(5), 694–702 (2016).
20. M. G. Woodcock, R. Lehmann, R. J. Cionni, M. Breen, and M. C. Scott, "Intraoperative aberrometry versus standard preoperative biometry and a toric IOL calculator for bilateral toric IOL implantation with a femtosecond laser: One-month results," J. Cataract Refractive Surg. **42**(6), 817–825 (2016).
21. N. Yesilirmak, S. Palioura, W. Culbertson, S. H. Yoo, and K. Donaldson, "Intraoperative wavefront aberrometry for toric intraocular lens placement in eyes with a history of refractive surgery," J. Refract. Surg. **32**(1), 69–70 (2016).
22. J. O. Huelle, V. Druchkiv, N. E. Habib, G. Richard, T. Katz, and S. J. Linke, "Intraoperative aberrometry-based aphakia refraction in patients with cataract: status and options," Br. J. Ophthalmol. **101**(2), 97–102 (2017).
23. R. R. Krueger, W. Shea, Y. Zhou, R. Osher, S. G. Slade, and D. F. Chang, "Intraoperative, real-time aberrometry during refractive cataract surgery with a sequentially shifting wavefront device," J. Refract. Surg. **29**(9), 630–635 (2013).
24. C. De Freitas, V. M. Hernandez, M. Ruggeri, H. A. Durkee, S. Williams, G. Gregori, A. Ho, F. Manns, and J.-M. Parel, "Simultaneous refraction measurement and OCT axial biometry of the eye during accommodation," Proc. SPIE **9693**, 969315 (2016).
25. J. C. He and J. Wang, "Measurement of wavefront aberrations and lens deformation in the accommodated eye with optical coherence tomography-equipped wavefront system," Opt. Express **22**(8), 9764–9773 (2014).
26. X. Mao, J. T. Banta, B. Ke, H. Jiang, J. He, C. Liu, and J. Wang, "Wavefront derived refraction and full eye biometry in pseudophakic eyes," PLoS One **11**(3), e0152293 (2016).
27. B. Hermann, E. J. Fernandez, A. Unterhuber, H. Sattmann, A. F. Fercher, W. Drexler, P. M. Prieto, and P. Artal, "Adaptive-optics ultrahigh-resolution optical coherence tomography," Opt. Lett. **29**(18), 2142–2144 (2004).

28. R. J. Zawadzki, S. M. Jones, S. S. Olivier, M. Zhao, B. A. Bower, J. A. Izatt, S. Choi, S. Laut, and J. S. Werner, "Adaptive-optics optical coherence tomography for high-resolution and high-speed 3D retinal in vivo imaging," Opt. Express **13**(21), 8532–8546 (2005).
29. Y. Zhang, J. Rha, R. Jonnal, and D. Miller, "Adaptive optics parallel spectral domain optical coherence tomography for imaging the living retina," Opt. Express **13**(12), 4792–4811 (2005).
30. M. Ruggeri, S. R. Uhlhorn, C. De Freitas, A. Ho, F. Manns, and J.-M. Parel, "Imaging and full-length biometry of the eye during accommodation using spectral domain OCT with an optical switch," Biomed. Opt. Express **3**(7), 1506–1520 (2012).
31. M. Ruggeri, C. de Freitas, S. Williams, V. M. Hernandez, F. Cabot, N. Yesilirmak, K. Alawa, Y. C. Chang, S. H. Yoo, G. Gregori, J. M. Parel, and F. Manns, "Quantification of the ciliary muscle and crystalline lens interaction during accommodation with synchronous OCT imaging," Biomed. Opt. Express **7**(4), 1351–1364 (2016).
32. D. Nankivil, G. Waterman, F. LaRocca, B. Keller, A. N. Kuo, and J. A. Izatt, "Handheld, rapidly switchable, anterior/posterior segment swept source optical coherence tomography probe," Biomed. Opt. Express **6**(11), 4516–4528 (2015).
33. M. Ruggeri, S. Williams, B. M. Heilman, Y. Yao, Y. C. Chang, A. Mohamed, N. G. Sravani, H. Durkee, C. Rowaan, A. Gonzalez, A. Ho, J. M. Parel, and F. Manns, "System for on- and off-axis volumetric OCT imaging and ray tracing aberrometry of the crystalline lens," Biomed. Opt. Express **9**(8), 3834–3851 (2018).
34. S. Norrby, "The Dubbelman eye model analysed by ray tracing through aspheric surfaces," Ophthalmic Physiol. Opt. **25**(2), 153–161 (2005).
35. T. Raasch, "Clinical refraction in three-dimensional dioptric space revisited," Optom. Vis. Sci. **74**(6), 376–380 (1997).
36. L. N. Thibos, W. Wheeler, and D. Horner, "Power vectors: an application of Fourier analysis to the description and statistical analysis of refractive error," Optom. Vis. Sci. **74**(6), 367–375 (1997).
37. J. M. Bland and D. G. Altman, "Measuring agreement in method comparison studies," Stat. Methods Med. Res. **8**(2), 135–160 (1999).
38. G. Smith, "Refraction and visual acuity measurements: what are their measurement uncertainties?" Clin. Exp. Optom. **89**(2), 66–72 (2006).
39. D. A. Goss and T. Grosvenor, "Reliability of refraction–a literature review," J. Am. Optom. Assoc. **67**(10), 619–630 (1996).
40. M. A. Bullimore, R. E. Fusaro, and C. W. Adams, "The repeatability of automated and clinician refraction," Optom. Vis. Sci. **75**(8), 617–622 (1998).
41. L. N. Davies, E. A. H. Mallen, J. S. Wolffsohn, and B. Gilmartin, "Clinical evaluation of the Shin-Nippon NVision-K 5001/Grand Seiko WR-5100 K autorefractor," Optom. Vis. Sci. **80**(4), 320–324 (2003).
42. E. A. Mallen, J. S. Wolffsohn, B. Gilmartin, and S. Tsujimura, "Clinical evaluation of the Shin-Nippon SRW-5000 autorefractor in adults," Ophthalmic Physiol. Opt. **21**(2), 101–107 (2001).
43. N. J. Durr, S. R. Dave, F. A. Vera-Diaz, D. Lim, C. Dorronsoro, S. Marcos, F. Thorn, and E. Lage, "Design and clinical evaluation of a handheld wavefront autorefractor," Optom. Vis. Sci. **92**(12), 1140–1147 (2015).
44. M. Rubio, C. S. Hernández, E. Seco, P. Perez-Merino, I. Casares, S. R. Dave, D. Lim, N. J. Durr, and E. Lage, "Validation of an affordable handheld wavefront autorefractor," Optom. and Vis. Sci. **96**(10), 726–732 (2019).
45. P. Bedggood, M. Daaboul, R. Ashman, G. Smith, and A. Metha, "Characteristics of the human isoplanatic patch and implications for adaptive optics retinal imaging," J. Biomed. Opt. **13**(2), 024008 (2008).
46. A. V. Dubinin, T. Y. Cherezova, A. I. Belyakov, and A. V. Kudryashov, "Isoplanatism of the optical system of the human eye," J. Opt. Tech. **75**(3), 172–174 (2008).
47. A. V. Goncharov, M. Nowakowski, M. T. Sheehan, and C. Dainty, "Reconstruction of the optical system of the human eye with reverse ray-tracing," Opt. Express **16**(3), 1692–1703 (2008).
48. M. Nowakowski, M. Sheehan, D. Neal, and A. V. Goncharov, "Investigation of the isoplanatic patch and wavefront aberration along the pupillary axis compared to the line of sight in the eye," Biomed. Opt. Express **3**(2), 240–258 (2012).
49. J. Tarrant and A. Roorda, "The extent of the isoplanatic patch of the human eye," Invest. Ophthalmol. Visual Sci. **47**, 1195 (2006).
50. B. Lee, S. Chen, E. M. Moult, Y. Yu, A. Y. Alibhai, N. Mehta, C. R. Baumal, N. K. Waheed, and J. G. Fujimoto, "High-Speed, ultrahigh-resolution spectral-domain OCT with extended imaging range using reference arm length matching," Transl. Vis. Sci. Technol. **9**(7), 12 (2020).